Schweizerischer Erdbebendienst
Service Sismologique Suisse
Servizio Sismico Svizzero
Servizi da Terratrembels Svizzer

ETH
Eidgenössische Technische Hochschule Zürich
Swiss Federal Institute of Technology Zurich

Sion - Mayennets (SIOM)

SITE CHARACTERIZATION REPORT

Clotaire MICHEL, Daniel ROTEN, Valerio POGGI,

Jan BURJANEK, Carlo CAUZZI, Donat FÄH

Sonneggstrasse 5 CH-8092 Zürich Switzerland; E-mail: clotaire.michel@sed.ethz.ch

Last modified : November 5, 2013

Abstract

This report presents the site characterization of the SIOM SSMNet station, renewed in 2011, located in the edge of the Rhone valley. Ambient vibration array measurements were performed in addition to existing array and single station noise measurements. It was found that the Rhone valley is behaving in a 2D fashion. The shape of the bedrock at the basin edge is assessed and velocity profiles are proposed for several locations, including for SIOM station. However, the 2D behaviour is limiting the capabilities of the employed techniques so that the results are uncertain. The SIOM site is characterized by $25\,\mathrm{m}$ of poorly consolidated sediment on top of $125\,\mathrm{m}$ of more consolidated sediments with a velocity of $600\,\mathrm{m/s}$. The bedrock was found at $150\,\mathrm{m}$ depth with a velocity of $1500\,\mathrm{m/s}$. $V_{s,30}$ is found to be $365\,\mathrm{m/s}$, corresponding to ground type C in the Eurocode 8. These inverted profiles could help improving the numerical models of the Rhone valley. These 2D and 3D models are necessary to correctly reproduce the recorded ground motion at SIOM.

Contents

1 Introduction

The station SIOM (Sion Mayennets) is part of the Swiss Strong Motion Network (SSMNet) in Sion. It was renewed in 2011 in the frame of the SSMNet Renewal project. This project includes also the site characterization. The passive array measurement technique has been selected as a standard tool to investigate these sites. Extensive single station measurement campaigns have been performed between 2003 and 2006 in the city of Sion [Roten, 2007, Fritsche, 2008]. Moreover, array measurements were performed in 2005 by H.B. Havenith close to the site of the SSMNet station. The authors of this report performed another array during the night between the 23rd and the 24th June 2011 at the station site (Fig. 1), southern from the previous array. This report presents the measurement setup of the 2 arrays, the results of the H/V analysis and of the array processing of the surface waves (dispersion curves). Inversions of these results into velocities are performed in order to determine the velocity profile at the station site. Finally, several parameters are derived to predict site amplification at SIOM.

Canton	City	Location	Station code	Site type	Slope
Valais	Sion	Mayennets	SIOM	Basin edge	Slight slope

Table 1: Main characteristics of the study-site.

Figure 1: Picture of the site.

2 Experiment description

2.1 Ambient Vibrations

The ground surface is permanently subjected to ambient vibrations due to:

- natural sources (ocean and large-scale atmospheric phenomena) below $1\,\mathrm{Hz}$,
- local meteorological conditions (wind and rain) at frequencies around $1\,\mathrm{Hz}$,
- human activities (industrial machines, traffic…) at frequencies above $1\,\mathrm{Hz}$ [Bonnefoy-Claudet et al., 2006].

The objective of the measurements is to record these ambient vibrations and to use their propagation properties to infer the underground structure. First, the polarization of the recorded waves (H/V ratio) is used to derive the resonance frequencies of the soil column. Second, the arrival time delays at many different stations are used to derive the velocity of surface waves at different frequencies (dispersion). The information (H/V, dispersion curves) is then used to derive the properties of the soil column using an inversion process.

2.2 Equipment

For the measurements performed in 2005 (called ASIOM) and in 2011 (called SIO), 4 and 12 Quanterra Q330 dataloggers named NR01 to NR12, respectively, connected to respectively 8 and 14 Lennartz 3C 5 s seismometers, respectively, were available (see Tab. 2). In 2005, an additional Mars88 was present and recorded at the central point. This too short recording was however not used here. Each Q330 datalogger can record on 2 ports A (channels EH1, EH2, EH3 for Z, N, E directions) and B (channels EH4, EH5, EH6 for Z, N, E directions). The time synchronization was ensured by GPS. The sensors are placed on a metal tripod generally on the asphalt for these arrays.

Digitizer	**Model**	**Number**	**Resolution**
	Quanterra Q330	4	$24\,\mathrm{bits}$
	Quanterra Q330	12	$24\,\mathrm{bits}$
Sensor type	**Model**	**Number**	**Cut-off frequency**
Velocimeter	Lennartz 3C	8	$0.2\,\mathrm{Hz}$
Velocimeter	Lennartz 3C	14	$0.2\,\mathrm{Hz}$

Table 2: Equipment used.

2.3 Geometry of the arrays

The ASIOM array includes 2 cross-shape configurations following the main streets. The minimum inter-station distance and the aperture are 15 and $320\,\mathrm{m}$, respectively. The array configuration for SIO includes 3 rings of 10, 25 and $60\,\mathrm{m}$ radius around a central station with 3, 5 and

5 sensors, respectively, i. e. with a total of 14 sensors. The minimum inter-station distance and the aperture are therefore 10 and 120 m. The experimental setups are displayed in Fig. 2 and Fig. 3. The final usable datasets are detailed in section 3.2.
Man-made terraces to compensate the slope are present parallel to the valley where the array SIO was set. This may have influenced the recordings.

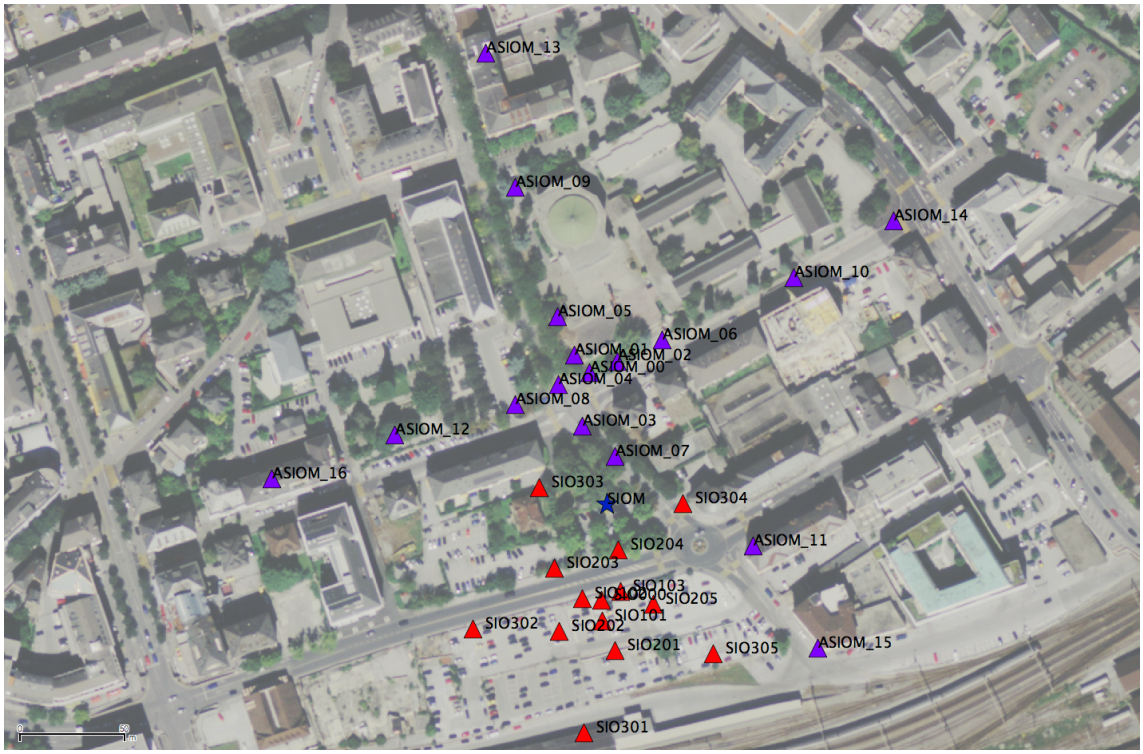

Figure 2: Map of the 2011 SIO (red triangles) and 2005 ASIOM (purple triangles) arrays in Sion city centre, close to SSMNet station SIOM (blue star).

2.4 Positioning of the stations

The sensor coordinates of the ASIOM array were measured using a NOVATEL differential GPS using a base station and a rover.

The positioning of the SIO stations was performed using a differential GPS device (Leica Viva), including only a rover station and using the Real Time Kinematic technique provided by Swisstopo. It allows an absolute positioning with an accuracy of about 3 cm on the Swissgrid.

Figure 3: Geometry of the SIO array.

3 Data quality

3.1 Usable data

The largest time windows were extracted, for which all the sensors of the array were in position and the GPS synchronization was ensured. For ASIOM, two datasets were extracted from the first configuration with 7 and 8 points, respectively. However, the dataset with 8 points is two short for processing.

For the SIO array, two datasets were extracted, either in maximizing the recording duration or in optimizing the quality, keeping only the last hour that was more quiet. The first strategy is kept in the following. The characteristics of these datasets are detailed in Tab. 3.

ASIOM array was performed during day time along main roads and is therefore very noisy. SIO array was performed during the night, but the surroundings were not perfectly quiet during the recording, especially many cars went through the array.

3.2 Data processing

The data were first converted to SAC format including in the header the sensor coordinates (CH1903 system), the recording component and a name related to the position. For ASIOM array, points are called ASIOM_XX with XX from 01 to 16. For SIO array, the name is made of 3 letters characterizing the location (SIO here), 1 digit for the ring and 2 more digits for the number in the ring. Recordings were not corrected from the instrumental response.

Dataset	Starting Date	Time	Length	F_s	Min. inter-distance	Aperture	# of points
ASIOM1 7	2005/05/11	09:46	52 min	200 Hz	15 m	75 m	7
ASIOM1 8	2011/05/11	11:00	28 min	200 Hz	15 m	75 m	8
ASIOM2	2011/05/11	12:33	57 min	200 Hz	55 m	320 m	8
SIO long	2011/06/23	21:49	190 min	200 Hz	10 m	120 m	14
SIO short	2011/06/23	23:56	63 min	200 Hz	10 m	120 m	14

Table 3: Usable datasets.

4 H/V processing

4.1 Processing method and parameters

In order to process the H/V spectral ratios, several codes and methods were used. The classical H/V method was applied using the Geopsy `http://www.geopsy.org` software. In this method, the ratio of the smoothed Fourier Transform of selected time windows are averaged. Tukey windows (cosine taper of 5% width) of $50\,\mathrm{s}$ long overlapping by 50% were selected. Konno and Ohmachi [1998] smoothing procedure was used with $b = 80$. The classical H/V method of Fäh et al. [2001] was also applied.

Moreover, the time-frequency analysis method [Fäh et al., 2009] was used to estimate the ellipticity function more accurately using the Matlab code of V. Poggi. In this method, the time-frequency analysis using the Wavelet transform is computed for each component. For each frequency, the maxima over time (10 per minute with at least $0.1\,\mathrm{s}$ between each) in the TFA are determined. The Horizontal to Vertical ratio of amplitudes for each maximum is then computed and statistical properties for each frequency are derived. Cosine wavelet with parameter 9 was used. The mean of the distribution for each frequency is stored. For the sake of comparison, the time-frequency analysis of Fäh et al. [2001], based on the spectrogram, was also used, as well as the wavelet-based TFA coded in Geopsy.

The ellipticity extraction using the Capon analysis [Poggi and Fäh, 2010] was also performed and displayed on Fig. 5 (See section on array analysis for details).

Method	Freq. band	Win. length	Anti-trig.	Overlap	Smoothing
Standard H/V Geopsy	$0.2 - 20\,\mathrm{Hz}$	$50\,\mathrm{s}$	No	50%	K&O 80
Standard H/V D. Fäh	$0.2 - 20\,\mathrm{Hz}$	$30\,\mathrm{s}$	No	75%	?
H/V TFA Geopsy	$0.2 - 20\,\mathrm{Hz}$	Morlet m=8 fi=1	No	-	?
H/V TFA D. Fäh	$0.2 - 20\,\mathrm{Hz}$	Specgram	No	-	?
H/V TFA V. Poggi	$0.2 - 20\,\mathrm{Hz}$	Cosine wpar=9	No	-	No

Table 4: Methods and parameters used for the H/V processing.

4.2 Results of the SIO array

The results for the SIO array show homogeneous H/V ratios. The peak is well defined around $0.46\,\mathrm{Hz}$ (Fig. 4). At $8.3\,\mathrm{Hz}$, a large industrial peak, visible as a sharp spike in unsmoothed spectra, disturbs the H/V ratios on all recordings. Point SIO303 deviates from the other points between 0.5 and $2\,\mathrm{Hz}$ and should not be used. Using the Time-Frequency analysis does not change much the picture but smoothes the low frequency part (Fig. 4 bottom). The comparison of all available methods is displayed on point SIO000 (Fig. 5), in which the classical methods were divided by $\sqrt{2}$ to account for Love waves contribution [Fäh et al., 2001]. In this case, this division would not have been necessary, indicating that few Love waves are present. The matching above the resonance frequency is good except smoothing issues. The 3C FK analysis provides lower values above $2\,\mathrm{Hz}$. Between 1 and $2\,\mathrm{Hz}$, peaks at 1.03 and $1.25\,\mathrm{Hz}$ can be seen,

as well in other displayed curves. Due to the limited aperture of the array, no energy below $1\,\mathrm{Hz}$ can be retrieved.

4.3 Polarization analysis

Considering the shape of the Rhone basin and previous research [Roten, 2007, Roten et al., 2008], a 2D resonance is very likely to occur at SIOM site. Therefore, polarization analysis on the array data was performed using the method of Burjánek et al. [2010]. All points (Fig. 6) show a clear polarization at $0.5\,\mathrm{Hz}$ in the direction of the valley axis, which confirms that this resonance frequency is related to 2D behaviour of the valley.

The fundamental frequency at SIOM station is therefore $0.46\,\mathrm{Hz}$ and corresponds to the fundamental SH mode of the 2D resonance of the Rhone valley and is therefore not related to the bedrock depth at SIOM. The ellipticity curve should therefore not be used in the 1D inversion. The small peaks at 1.03 and $1.25\,\mathrm{Hz}$ observed on Fig. 5 are likely to be higher modes of the 2D resonance.

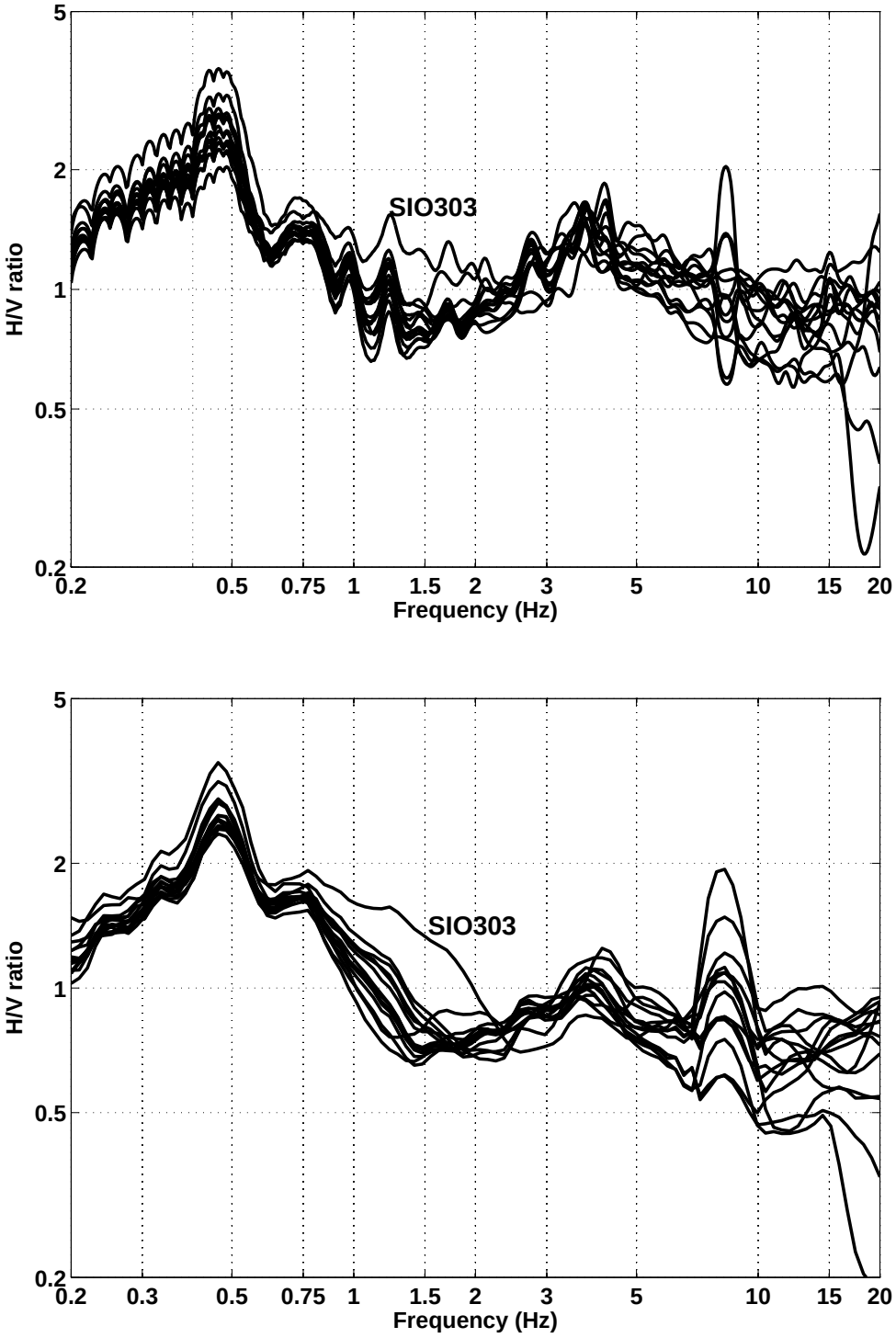

Figure 4: H/V spectral ratios of SIO array using the standard method (Geopsy - top) and the TFA method (code V: Poggi - bottom).

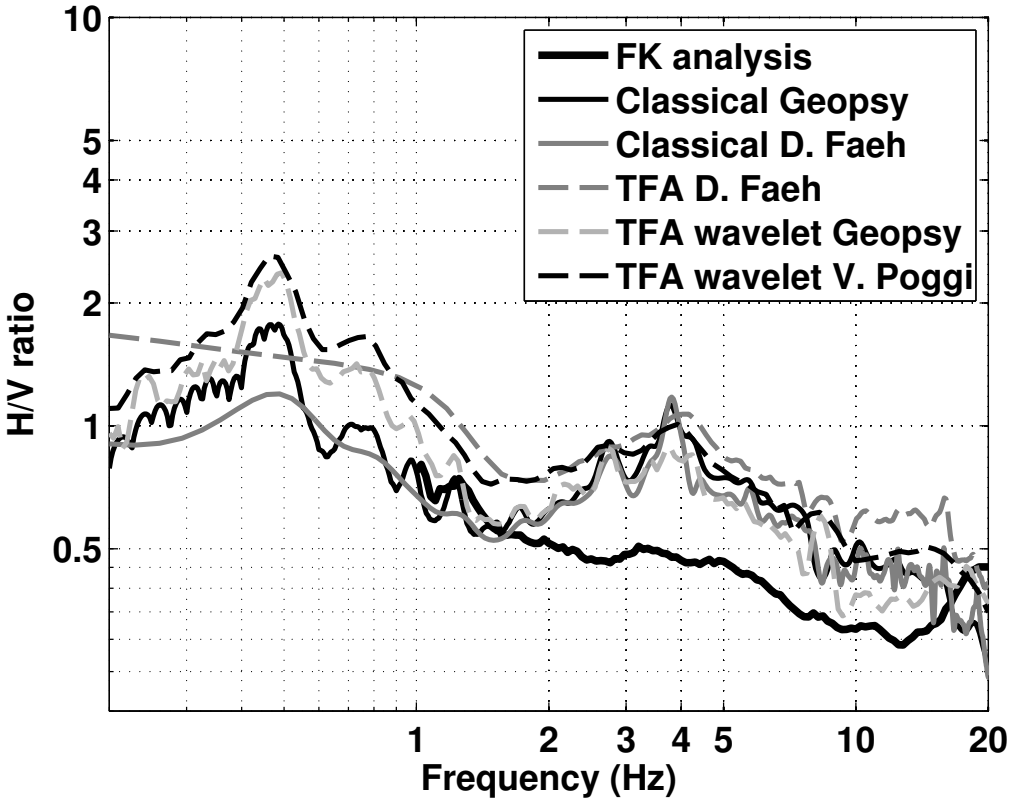

Figure 5: H/V spectral ratios using all available methods at point SIO000 (central point of the array). Classical methods were divided by $\sqrt{2}$ that is too much in this case.

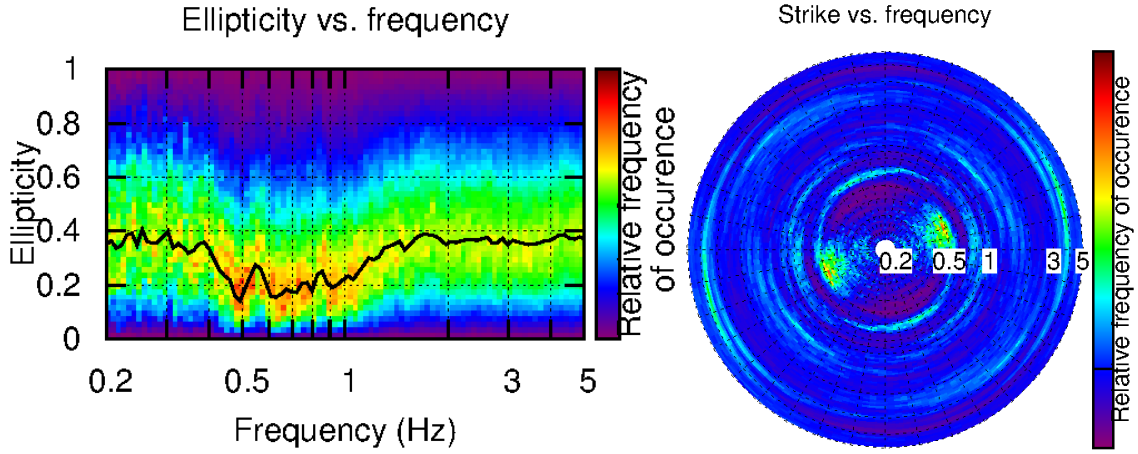

Figure 6: Polarization analysis at point SIO000. Left: Ellipticity (A trough in the ellipticity corresponds to polarized motion). Right: Strike of the polarization.

4.4 Results of the ASIOM array and cross-section of the valley

The H/V curves using the time-frequency analysis (code VP) of ASIOM recording points were compared to those of the SIO array data and at a long term test station at the SIOM station site (Fig. 7). It should be emphasized that traditional H/V method is not able to draw any tendency from the ASIOM recordings. Fig. 8 shows the evolution of H/V curve in the North/South direction, i.e. perpendicular to the valley. The quality at low frequency is poor for the ASIOM array (short duration, daytime measurement...).

The same peak around $0.46\,\mathrm{Hz}$, related to the 2D resonance, is found but it shows also a rapid change of the right flank of the ellipticity curves. All points in SIO array show a similar H/V except SIO303, similarly, all points of ASIOM array but the branch going to the South show comparable H/V. One can note that quality of H/V curves for ASIOM array is not good enough to see the $0.46\,\mathrm{Hz}$ but it is highly probable that it is still visible. It means the bedrock is dipping very fast between the centers of these two arrays as shown by the existing literature (Fig. 10). The 1D peaks were obtained in following roughly the right flank of the ellipticity. In the central part of the valley, it is not possible to peak anything else but the 2D resonance peak. The troughs at the end of the right flank were peaked as well. All results were projected along a -30°N line, from N to S and displayed on Fig. 9.

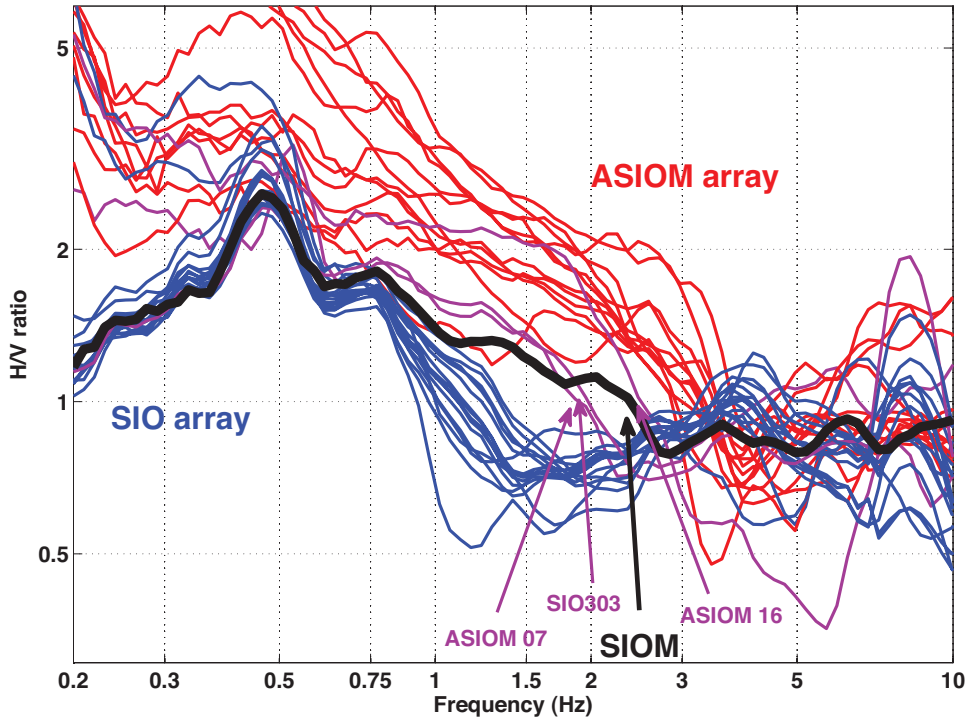

Figure 7: H/V curves of the SIO and ASIOM array together with SSMNet SIOM site.

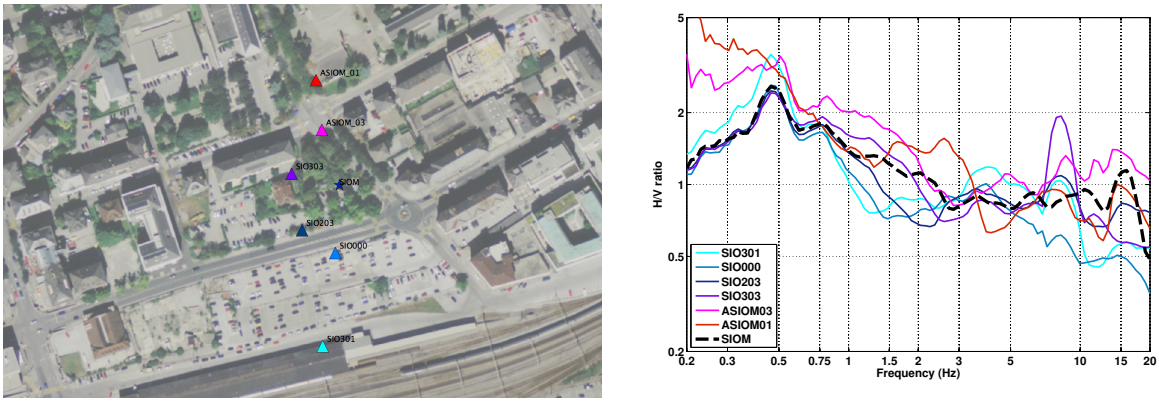

Figure 8: H/V cross-section of the city-centre of Sion.

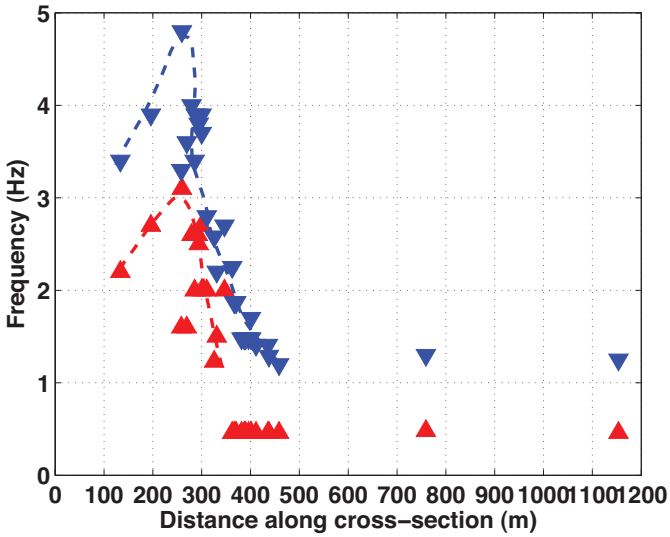

Figure 9: H/V cross-section of the city-centre of Sion (blue: troughs in H/V curve, red: peaks in H/V curve).

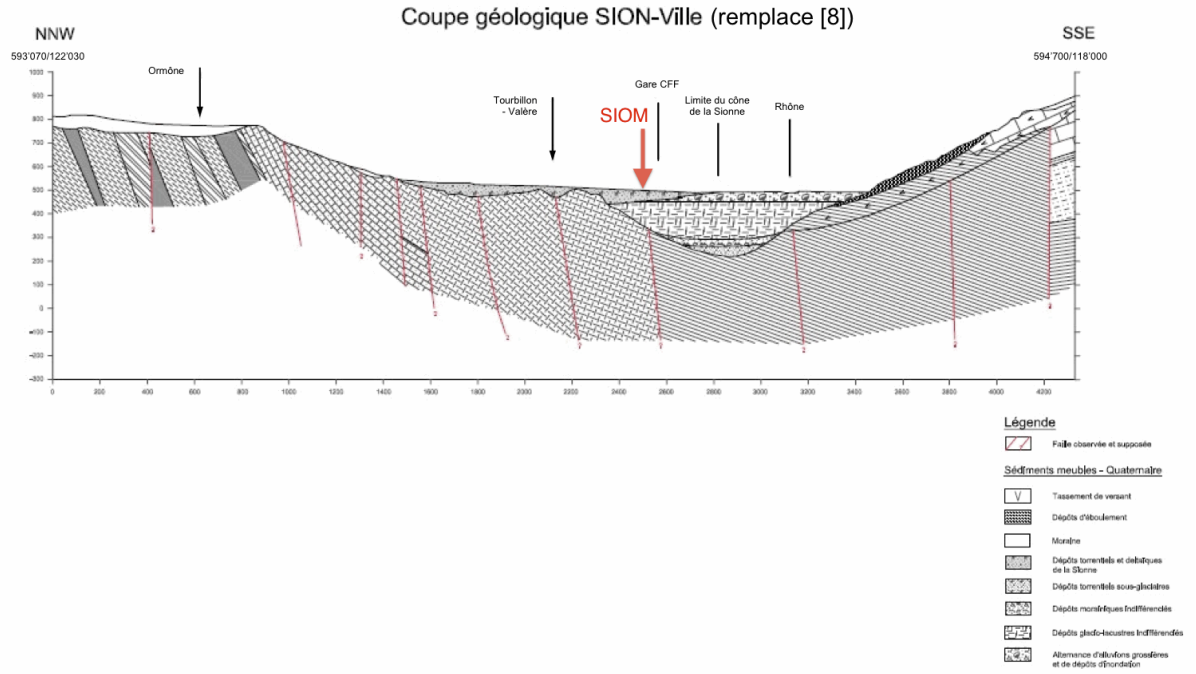

Figure 10: Geological cross-section of the city-centre of Sion [GéoVal Ingénieurs, 2011].

5 Array processing

5.1 Processing methods and parameters

The vertical components of the arrays were processed using the High-resolution FK analysis [Capon, 1969] using the Geopsy `http://www.geopsy.org` software. Better results were obtained using large time windows (100T, where T stands for period). The obtained dispersion curves were concatenated.

Moreover, a 3C array analysis [Fäh et al., 2008] was also performed using the 3C analysis tool [Poggi and Fäh, 2010]. It allows to derive Rayleigh and Love modes as well as ellipticity. The results of computations of both datasets were assembled to estimate the dispersion curves.

Method	Set	Freq. band	Win. length	Anti-trig.	Overlap	Grid step	Grid size	# max.
1C	SIO long	$0.5-20$ Hz	$100T$	No	50%	0.003	0.4	5
3C	SIO long	$0.5-20$ Hz	$30T$	No	5%	300	1500	5
			Tap. 0.1			m/s	m/s	
1C	ASIOM1 7	$1-25$ Hz	$100T$	No	50%	0.002	0.5	5
3C	ASIOM1 7	$2-25$ Hz	$20T$	No	5%	300	2500	5
			Tap. 0.1			m/s	m/s	
1C	ASIOM2	$1-25$ Hz	$100T$	No	50%	0.002	0.5	5
3C	ASIOM2	$2-25$ Hz	$20T$	No	5%	300	2500	5
			Tap. 0.1			m/s	m/s	

Table 5: Methods and parameters used for the array processing.

5.2 Results array SIO

The fundamental and first higher mode (Rayleigh) could be picked in the 1C FK analysis between 1 and 3.8 Hz and 4.5 and 15 Hz, respectively, but according to the array limit, only the part above 3 Hz (basically only the first higher mode) should be trusted (Fig. 11).

Using the 3C analysis, as previously, the fundamental and first higher Rayleigh modes can be picked (Fig. 12). The transverse and radial components do not provide any result. It was already clear from Fig. 5 that there was few energy for Love modes, which is confirmed here. It could be due to the proximity of the dipping bedrock or the absence of layering in the profile. 1C picked dispersion curve shows some differences with the 3C analysis due to the uncertain picking (Fig. 14).

A selection on the azimuth was performed in order to eventually detect velocity differences from waves entering the basin with respect to waves coming from the central part of the basin (waves entering the basin: $60-180\,^{\circ}$ counted anti-clockwise from the E direction, and $240-0\,^{\circ}$ for waves coming from the basin). Fig. 13 shows a different first higher mode for the waves entering the basin compared to the picked curve, eventually with higher velocities, but it remains questionable.

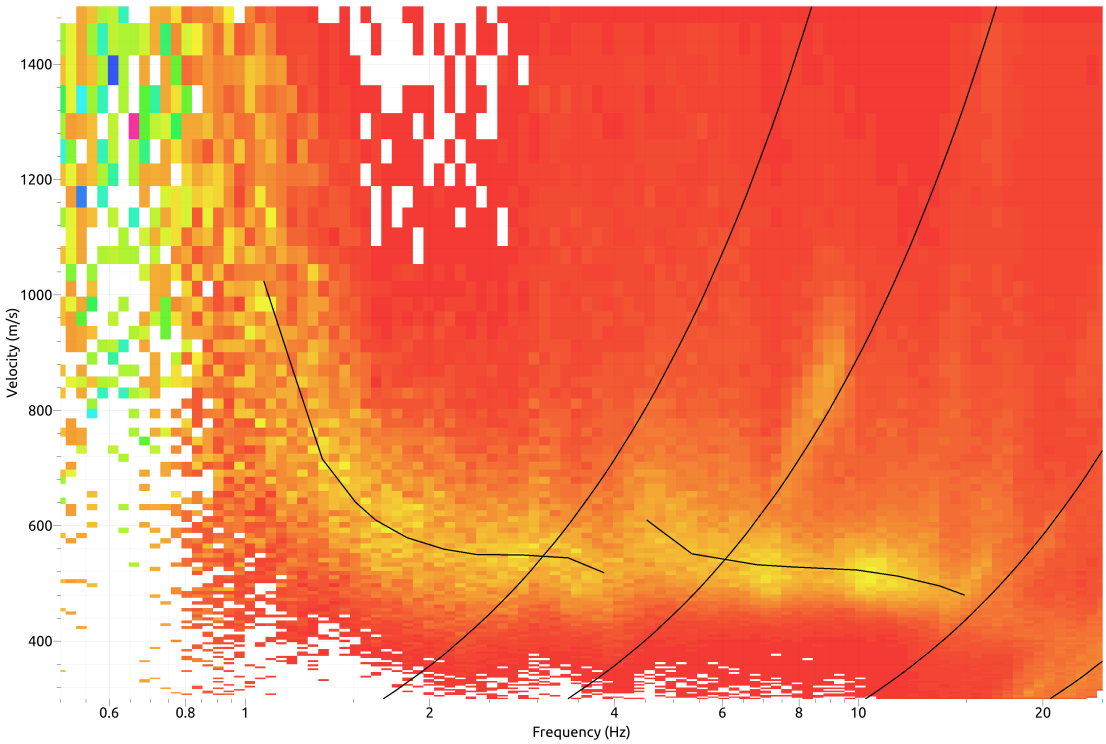

Figure 11: Dispersion curve obtained from the 1C array analysis of the SIO array.

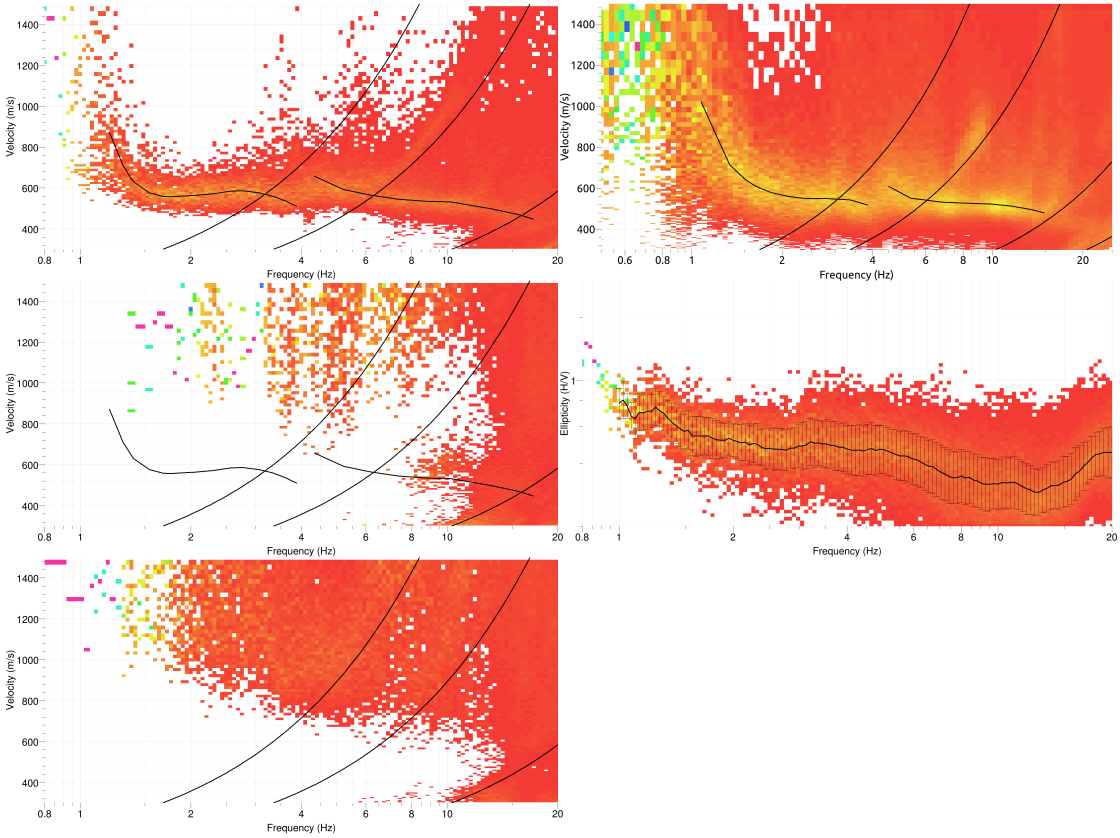

Figure 12: Results from the 3C array analysis of the SIO array. Top: vertical direction dispersion curve (left) and ellipticity (right); Centre: Radial component; Bottom: Transverse component.

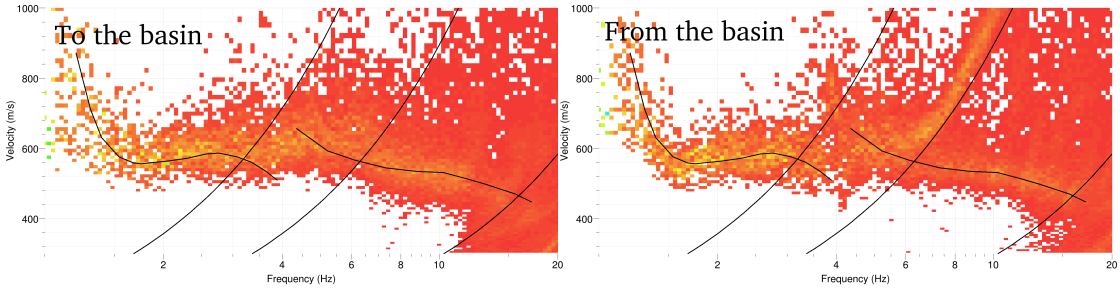

Figure 13: Histograms for selected azimuths for waves entering the basin (left) and coming from the basin (right) compared to the Rayleigh dispersion curves obtained from the analysis of all azimuths for SIO array.

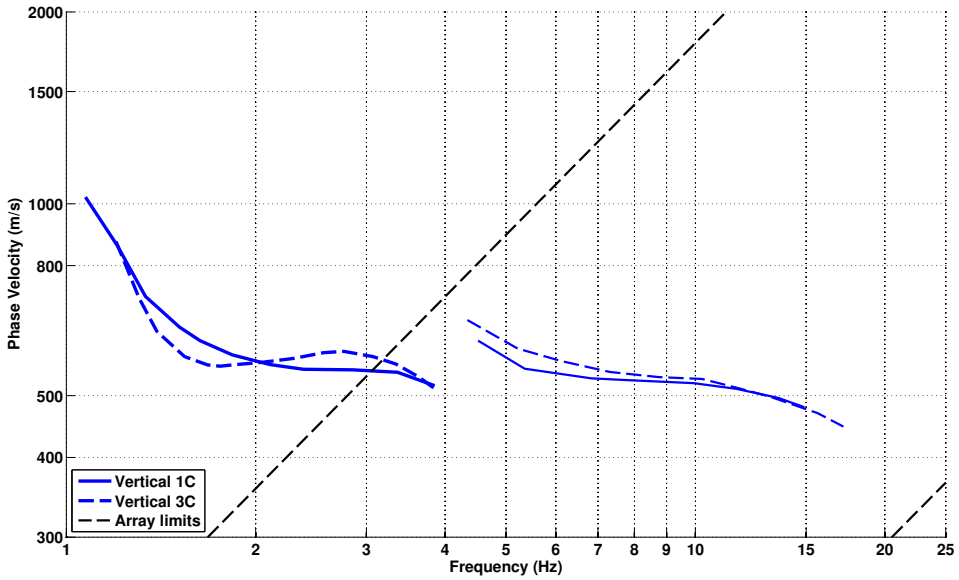

Figure 14: Comparison of obtained dispersion curves in the SIO array using 1C and 3C analyses for the Rayleigh modes.

5.3 Results array ASIOM

Although this array was already analyzed by H.B. Havenith, it was reprocessed for this report, the dispersion curve being not satisfactory. Array analysis was performed using the 1C and 3C HRFK method (Fig. 15 and Fig. 16). For the second configuration, the points 11 and 15, going to the South, were not used since they are on a very different geology. The Rayleigh mode could be extracted from 3 to $22\,\mathrm{Hz}$. The velocities range from 1500 down to $400\,\mathrm{m/s}$. The fundamental Love mode could also be extracted using the 3C analysis from 2.5 to $12\,\mathrm{Hz}$. The 3C analysis also allows to derive the ellipticity curve from 2 to $25\,\mathrm{Hz}$. It matches well with the TFA H/V. Fig. 17 shows a good match between the Rayleigh modes from the 1C and 3C arrays. Rayleigh curve from 1C analysis together with Love curve and ellipticity curve from the 3C will be used in the following.

The comparison of the Rayleigh dispersion curves between the SIO and ASIOM arrays can be found on Fig. 18. The resonance frequency of ASIOM, related to the rapid increase in velocity of the dispersion curve, is confirmed to be around $2.5\,\mathrm{Hz}$ and is clearly at higher frequency than the one of SIO. Moreover the surface layers of ASIOM and SIO seem to have the same velocities. The SIO array had a too small aperture to capture the deeper layers and therefore the sediment-bedrock interface. As a conclusion, the ASIOM array is representative for a shallower edge of the basin than the SIO array.

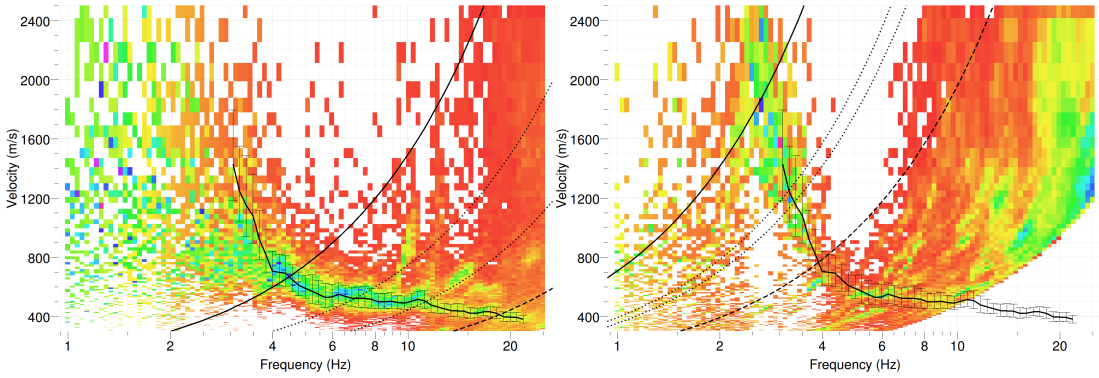

Figure 15: 1C analysis of the ASIOM array.

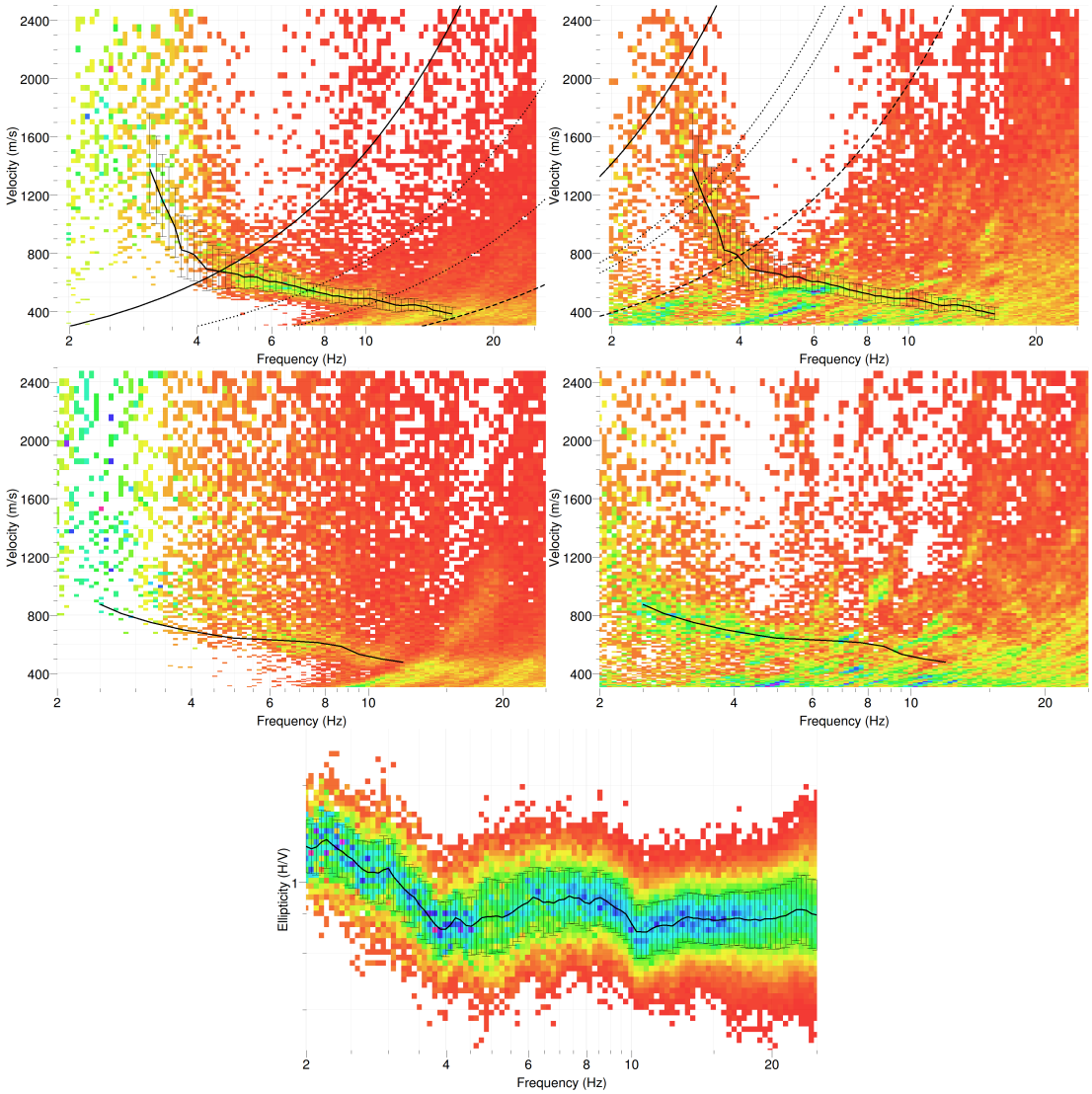

Figure 16: 3C analysis of the ASIOM array, including vertical (top) and transverse (centre) as well as the ellipticity (bottom), for the first (left) and the second (right) configuration.

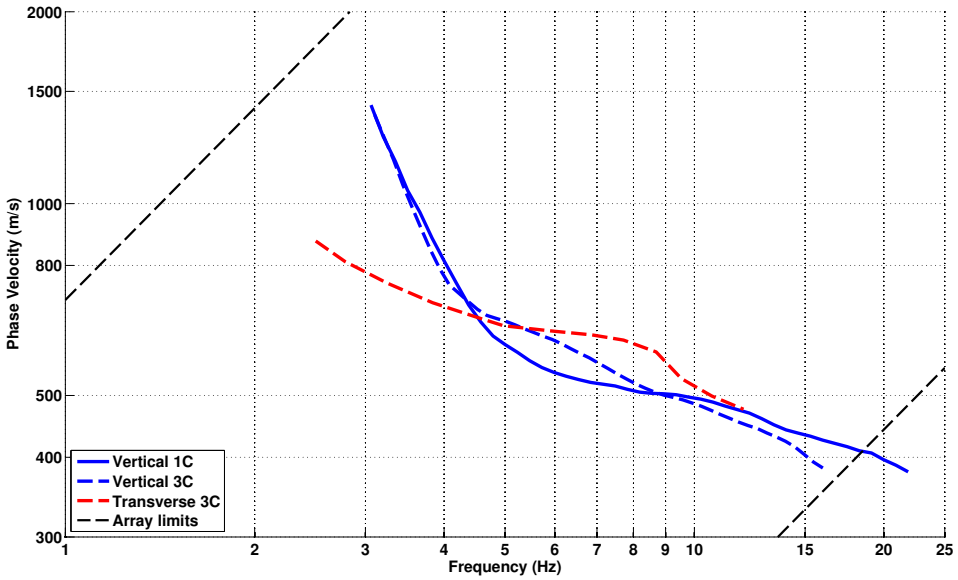

Figure 17: Comparison of obtained dispersion curves with the ASIOM array.

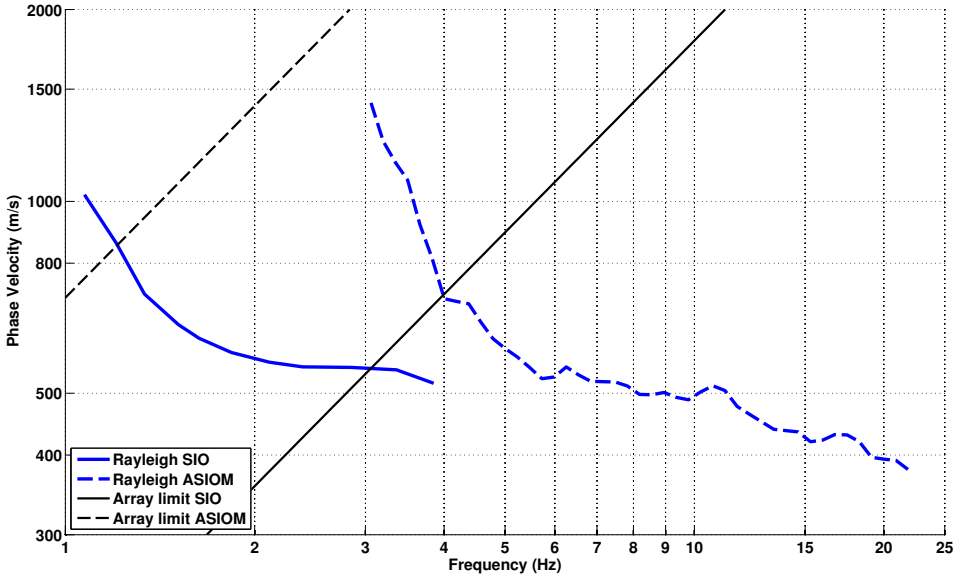

Figure 18: Comparison of obtained dispersion curves with the SIO and ASIOM arrays.

6 Inversion and interpretation

6.1 Inversion of ASIOM array

For the inversion, the Rayleigh (1C analysis $3 - 22\,\mathrm{Hz}$) and Love dispersion (3C analysis $2.5 - 12\,\mathrm{Hz}$) curves were used as targets, without standard deviation to avoid different weighting. The dispersion curve was resampled using 50 points between 1 and $30\,\mathrm{Hz}$ in log scale. Ellipticity from the 3C analysis ($2.2 - 25\,\mathrm{Hz}$), was also used as a simultaneous target with a weight of 0.1, again without standard deviation to avoid different weighting.

The inversion was performed using the Improved Neighborhood Algorithm (NA) [Wathelet, 2008] implemented in the Dinver software. In this algorithm, the tuning parameters are the following: Ns_0 is the number of starting models, randomly distributed in the parameter space, Nr is the the number of best cells considered around these Ns_0 models, Ns is the number of new cells generated in the neighborhood of the Nr cells (Ns/Nr per cell) and It_{max} is the number of iteration of this process. The process ends with $Ns_0 + Nr * \frac{Ns}{Nr} * It_{max}$ models. The used parameters are detailed in Tab. 6.

It_{max}	Ns_0	Ns	Nr
500	10000	100	100

Table 6: Tuning parameters of Neighborhood Algorithm.

During the inversion process, low velocity zones were not allowed. The Poisson ratio was supposed uniform on the whole profile (free parameter in the range 0.2-0.4) except the bottom layer and the density was supposed equal to $2000\,\mathrm{kg/m^3}$ except for the bottom layer ($2500\,\mathrm{kg/m^3}$). 3 layers are enough to explain the dispersion curve, but more layers are used to smooth the obtained results and better explore the parameter space.

The major resolved interface (Fig. 19), corresponding to the bedrock depth, is estimated at $70 \pm 10\,\mathrm{m}$. The velocity in the bedrock around $1500\,\mathrm{m/s}$ in this inversion, is however not clearly constrained. Roten et al. [2008] chose a value of $2325\,\mathrm{m/s}$ for the S-wave velocity in the bedrock and GéoVal Ingénieurs [2011] a value of $2200\,\mathrm{m/s}$. The uncertainty remains therefore high on this value. The next layer extends from 70 nearly up to $5\,\mathrm{m}$ with a constant velocity of about $600\,\mathrm{m/s}$. Above $5\,\mathrm{m}$, the velocity is decreasing down to $300\,\mathrm{m/s}$ on average.

When comparing to the target curve (Fig. 19), the curve is well represented by the inverted models. The ellipticity of the inverted models has a peak around $2.7\,\mathrm{Hz}$ and a trough around $3.7\,\mathrm{Hz}$ as seen on the observations. However, the inverted models show a higher amplitude ellipticity that can not be lowered with elastic models.

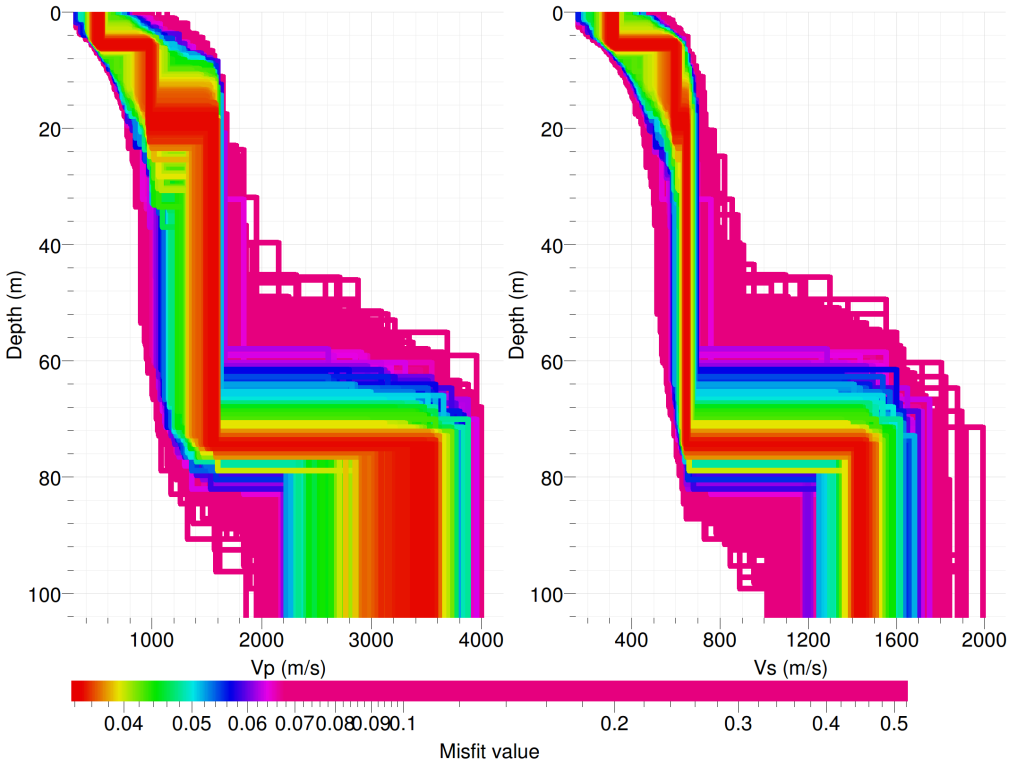

Figure 19: Inverted ground profiles in terms of V_p and V_s for the ASIOM array.

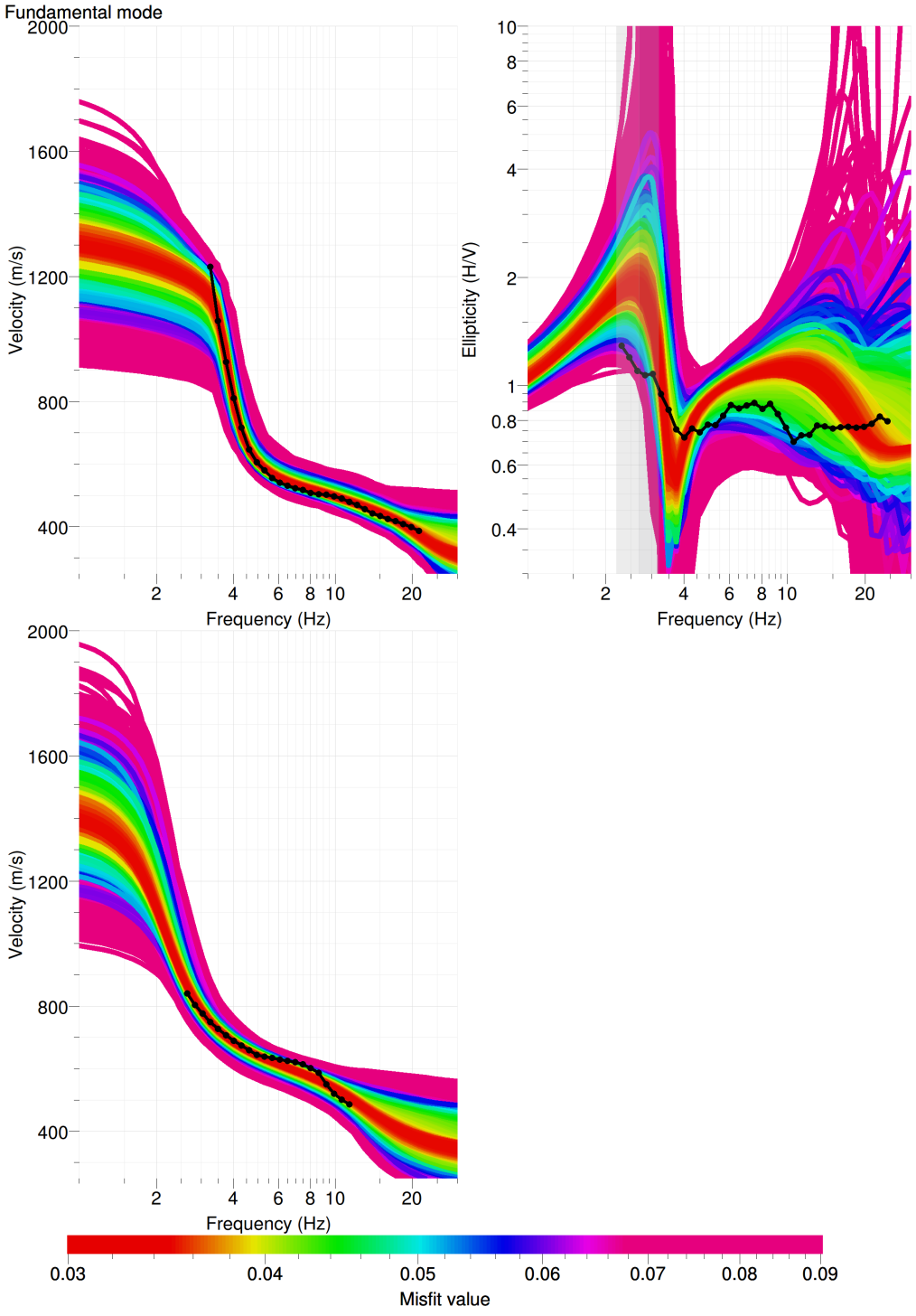

Figure 20: Comparison between inverted models and measured Rayleigh and Love modes (left), and ellipticity (right) for the ASIOM array.

6.2 Interpretation ASIOM array - bedrock depth at SIOM station

The geological model of GéoVal Ingénieurs [2011] is the latest available, with a cross-section located $60\,\mathrm{m}$ western from these measurements (Fig. 10). However, only boreholes down to $50\,\mathrm{m}$ depth were available to the authors and the bedrock interface was extracted from Rosselli [2001], which was shown not to be always accurate.

These results show that the bedrock depth at the shoulder on the edge of the deep Rhone basin is at $70\,\mathrm{m}$, i.e. not as shallow as provided by the geological cross-section, but in the uncertainty range provided by the authors (Fig. 10). These sedimentary layers are interpreted as alluvial deposits from the Sionne river.

In order to derive the bedrock depth on the basin edge, a constant velocity of $600\,\mathrm{m/s}$ in the sediments was assumed and the resulting bedrock depth was derived from the H/V peak frequency (Fig. 21). It gives a good idea of the location of the shoulder of the bedrock at the edge of the Rhone valley but does not provide information on the deep part since the resonance peak is related to the 2D resonance and therefore constant on the whole profile. The geological model [GéoVal Ingénieurs, 2011] is consistent with these results although the shoulder is found slightly deeper here. The basin centre, with 1D frequencies in theory even lower than the 2D resonance, is also found deeper than the geological cross-section in our study, but the constant velocity chosen here may not be representative for this part. The model of Roten et al. [2008], based on Frischknecht et al. [2005], is less realistic with an incorrect basin width and an overestimated basin depth. Fig. 21 shows also that the bedrock depth under SIOM station is in the order of $150\,\mathrm{m}$ and at about $180\,\mathrm{m}$ below the SIO array. These values are however still uncertain. As a comparison, from the geological profile, a depth of $140\,\mathrm{m}$ can be extracted at SIOM, $190\,\mathrm{m}$ depth at the train station. The model used by Resonance for the microzonation study, based on the geological model, is however slightly shallower ($110\,\mathrm{m}$ at SIOM, $125\,\mathrm{m}$ depth under the SIO array).

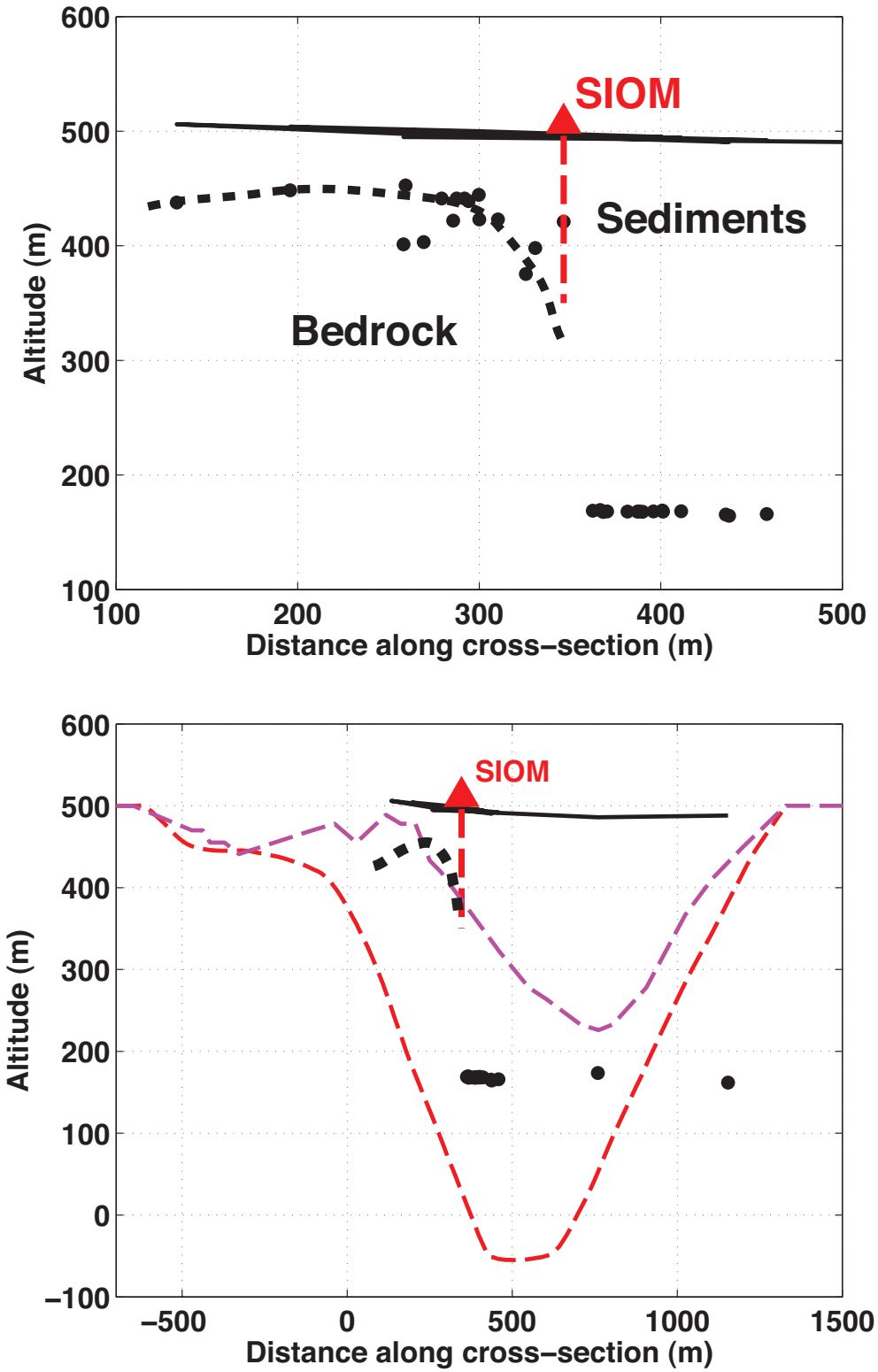

Figure 21: Cross-section of the city-centre of Sion in terms of bedrock depth. red: model from Roten et al. [2008]; magenta: model used by Resonance based on the geological model (Fig. 10); black dots and interpolation: H/V results.

6.3 Inversion of the SIO array

For the inversion of the SIO array, Rayleigh fundamental and first higher mode dispersion curves (3C analysis) were used as simultaneous targets. The curves were resampled using 50 points between 0.3 and $20\,\mathrm{Hz}$ in log scale. The ellipticity of the Rayleigh waves is displayed in the results but was not used in the inversion.

According to boreholes from the Valais roads, at least $45\,\mathrm{m}$ at the surface are gravels. In depth, according to the geological cross-section, lacustrine sediments are present, below $50\,\mathrm{m}$. This could result in a velocity inversion at $50\,\mathrm{m}$ or deeper. However, after testing, we found out that our data are too limited to constrain such an inversion. Therefore, during the inversion process, low velocity zones were not allowed. The bedrock velocity is set at $1500\,\mathrm{m/s}$, as found above, which turns out to be a good value when comparing to observation of amplification at the strong motion station. Higher velocities would lead to larger amplifications that are not observed. The bedrock depth has been set to $180\,\mathrm{m}$ depth. The Poisson ratio was inverted in each layer in the range 0.2-0.4, up to 0.47 just below the expected water table. The density was supposed equal to $2000\,\mathrm{kg/m^3}$ except for the deepest layer ($2500\,\mathrm{kg/m^3}$). Inversions with free layer depths as well as fixed layer depths were performed. 3 layers are enough to explain most of the targets (dispersion and ellipticity), but more layers are used to smooth the obtained results and better explore the parameter space. 5 independent runs of 5 different parametrization schemes (4 and 5 layers over a half space and 10, 11 and 12 layers with fixed depth) were performed. For further elaborations, the best models of these 25 runs were selected (Fig. 25).

The profiles found are very simple and all identical. They show a first layer of $25\,\mathrm{m}$ depth with a velocity of $340\,\mathrm{m/s}$ and a second layer down to the bedrock with a velocity of $600\,\mathrm{m/s}$. As set, the bedrock is located at $180\,\mathrm{m}$ with the imposed velocity of $1500\,\mathrm{m/s}$.

When comparing to the target curves (Fig. 23 and Fig. 24), the first higher mode, the only really clear in the array analysis is well represented. The fundamental is not well reproduced, but it was located out of the array limit and its shape may indicate that it results from a mix with the first higher mode.

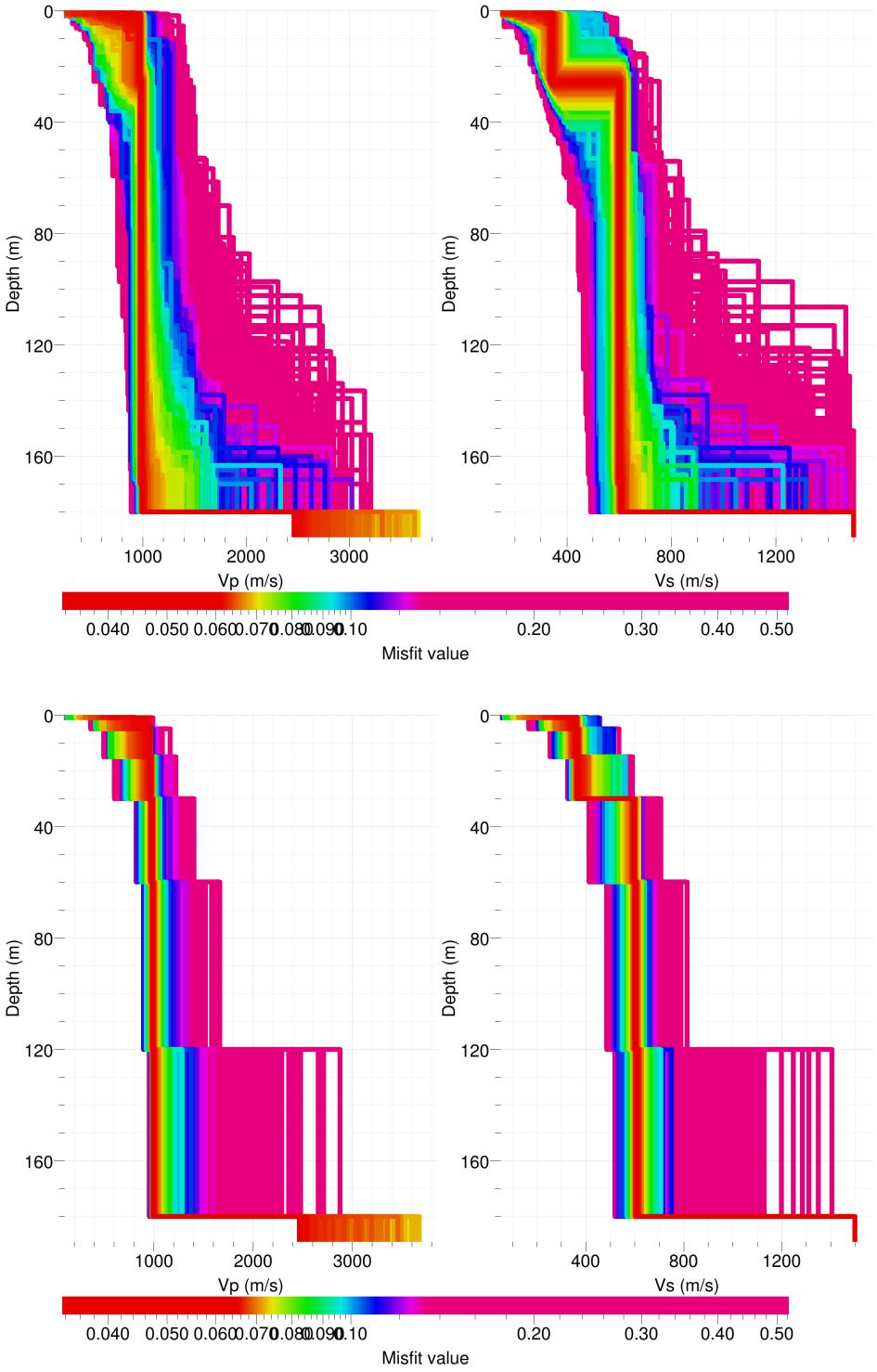

Figure 22: Inverted ground profiles in terms of V_p and V_s; top: free layer depth strategy; bottom: fixed layer depth strategy.

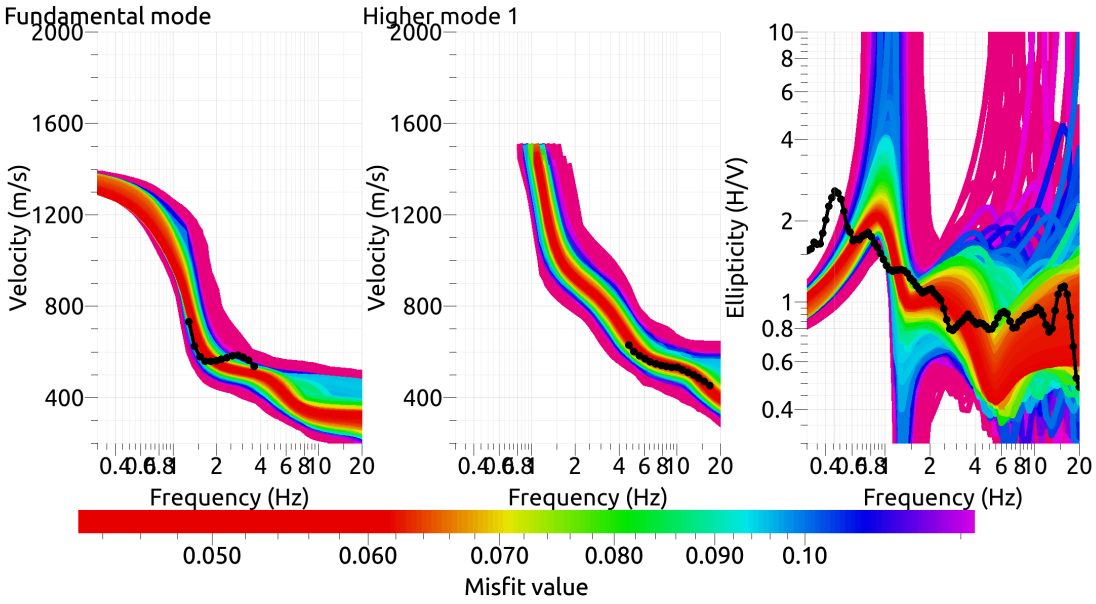

Figure 23: Comparison between inverted models and measured Rayleigh and corresponding ellipticity, free layer depth strategy.

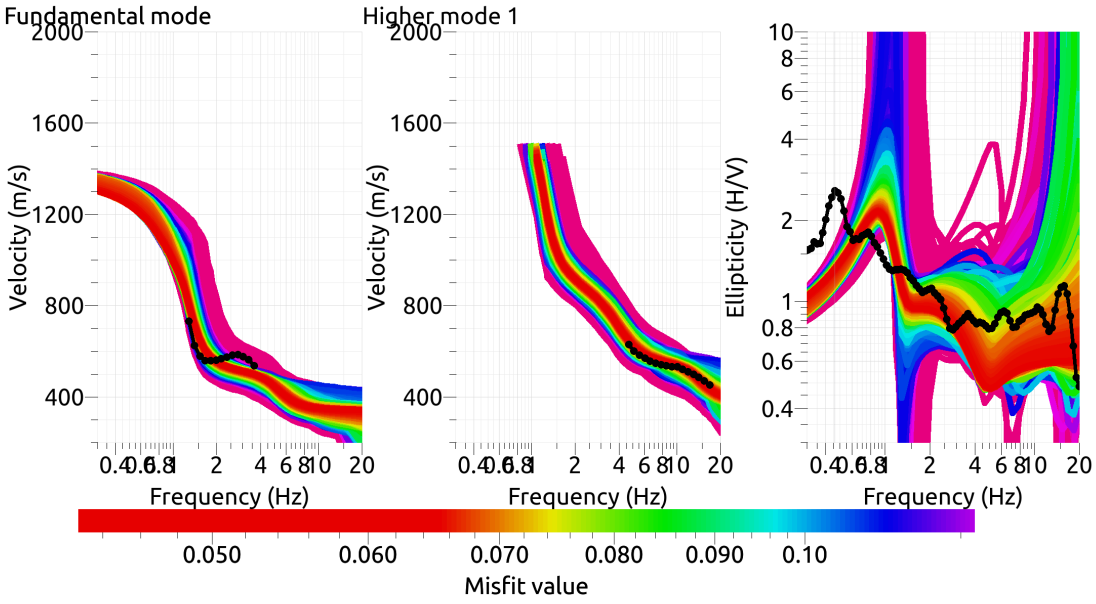

Figure 24: Comparison between inverted models and measured Rayleigh modes and corresponding ellipticity, fixed layer depth strategy.

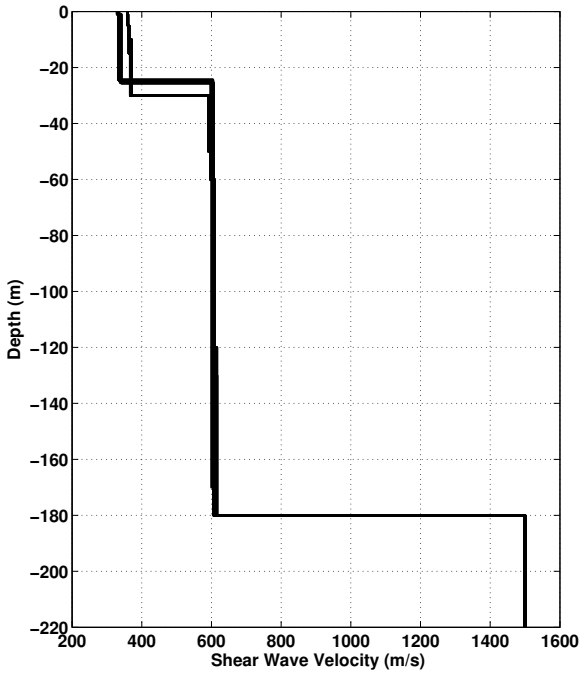

Figure 25: V_s ground profiles for the 25 best models fro SIO inversion.

6.4 Synthetic models for SIOM station

It was previously found that the bedrock at SIOM station was $30\,\mathrm{m}$ shallower than at SIO array. Therefore, $30\,\mathrm{m}$ thickness was removed from the lowest sediment layer of the best models of the SIO inversion (Fig. 26) to obtain the profiles at SIOM station. All further computations are based on these profiles.

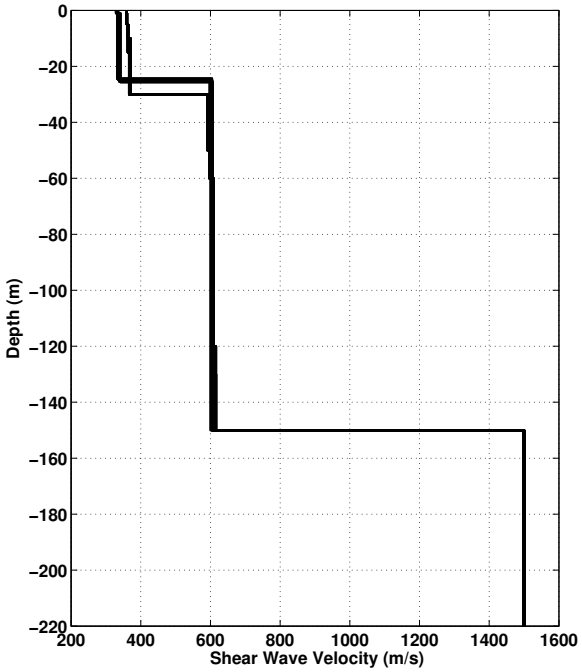

Figure 26: V_s ground profiles for the selected 25 best models for SIOM station.

6.5 Travel time average velocities and soil class

The distribution of the travel time average velocities at different depths was computed from the synthetic models at the SIOM station. Uncertainty is provided as one standard deviation of the selected profile but is not significant since they are all similar. $V_{s,30}$ is found to be $365\,\mathrm{m/s}$, meaning the site can be classified as class C in the Eurocode 8 CEN [2004] and in the Swiss Code SIA261 [SIA, 2003]. The classification for EC8 is conservative with respect to the purely mathematical result. For the ASIOM site, representative for the basin edge, $V_{s,30}$ has a value of $525\,\mathrm{m/s}$.

6.6 Quarter-wavelength velocity

The quarter-wavelength velocity approach [Joyner et al., 1981] provides, for a given frequency, the average velocity at the corresponding depth (Fig. 27). It is useful to identify the frequency

	Mean (m/s)	**Uncertainty (m/s)**
$V_{s,5}$	350	13
$V_{s,10}$	351	13
$V_{s,20}$	353	15
$V_{s,30}$	365	2
$V_{s,40}$	404	2
$V_{s,50}$	432	1
$V_{s,100}$	504	1
$V_{s,150}$	534	2
$V_{s,200}$	-	-

Table 7: Travel time averages at different depths from the synthetic 1D model for SIOM station.

limits of the experimental data (minimum frequency in the dispersion curves $1.3\,\mathrm{Hz}$). The results using this proxy show that dispersion curves are controlling the results until $100\,\mathrm{m}$ depth. The first higher mode only controls the profile down to $30\,\mathrm{m}$ depth only.
Moreover, the theoretical SH transfer function [Roesset, 1970] is computed from the inverted profiles. It is compared to the quarter-wavelength impedance contrast that is a proxy for amplification, that however cannot take resonances into account [Joyner et al., 1981] (Fig. 28). The synthetic SH transfer functions show peaks at resonance frequencies corresponding to the 1D bedrock depth, for instance at 1, 2.7 and $4.3\,\mathrm{Hz}$ etc. for the SIOM station. However, these 1D results are not reliable since the behaviour of the Rhone basin is driven by 2D effects.

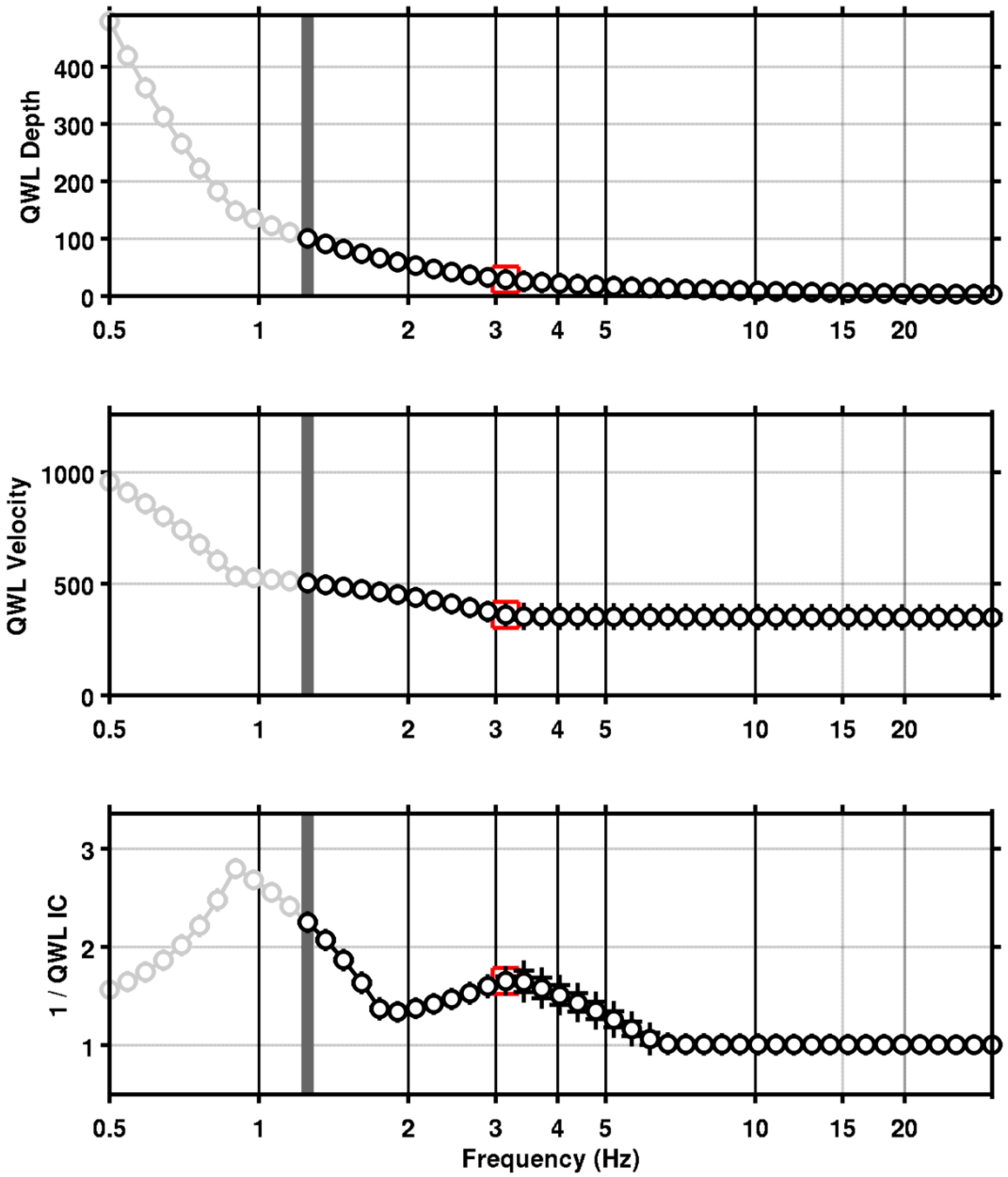

Figure 27: Quarter wavelength velocity representation of the velocity profile at SIOM (top: depth, centre: velocity, bottom: inverse of the impedance contrast). Black curve is constrained by the dispersion curves, light grey is not constrained by the data. Red square is corresponding to $V_{s,30}$.

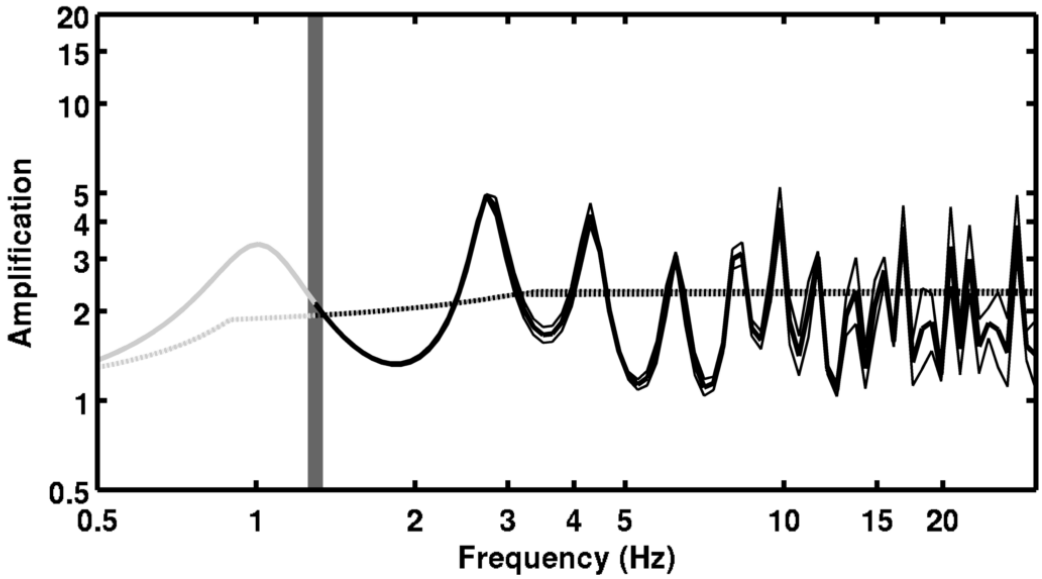

Figure 28: Theoretical SH transfer function (solid line) and quarter wavelength impedance contrast (dashed line) at SIOM with their standard deviation. Significance of the greyshades is detailed in Fig. 27.

7 Conclusions

As a conclusion, SIOM site is located at the basin edge of the Rhone valley that is behaving in a 2D fashion. The shape of the bedrock at the basin edge has been assessed with the ambient vibration data and velocity profiles have been proposed at several locations, including at SIOM station. However, the 2D behaviour is limiting the capabilities of the employed techniques so that the results are uncertain. The SIOM site is characterized by $25\,\mathrm{m}$ of poorly consolidated sediment on top of $125\,\mathrm{m}$ of more consolidated sediments with a velocity of $600\,\mathrm{m/s}$. The bedrock was found at $150\,\mathrm{m}$ depth with a velocity of $1500\,\mathrm{m/s}$, which seems low compared to the expected values, maybe due to weathering. $V_{s,30}$ is found to be $365\,\mathrm{m/s}$, corresponding to ground type C in the Eurocode 8. These inverted profiles could help improving the numerical models of the Rhone valley. These 2D and 3D models are necessary to correctly reproduce the recorded motion at SIOM.

Acknowledgements

The authors thanks Remo Grolimund for the help during these measurements and Corinne Lacave who provided the documentation used during the microzonation study.

References

Sylvette Bonnefoy-Claudet, Fabrice Cotton, and Pierre-Yves Bard. The nature of noise wavefield and its applications for site effects studies. *Earth-Science Reviews*, 79(3-4): 205–227, December 2006. ISSN 00128252. doi: 10.1016/j.earscirev.2006.07.004. URL http://linkinghub.elsevier.com/retrieve/pii/S0012825206001012.

Jan Burjánek, Gabriela Gassner-Stamm, Valerio Poggi, Jeffrey R. Moore, and Donat Fäh. Ambient vibration analysis of an unstable mountain slope. *Geophysical Journal International*, 180(2):820–828, February 2010. ISSN 0956540X. doi: 10.1111/j.1365-246X.2009.04451.x. URL http://doi.wiley.com/10.1111/j.1365-246X.2009.04451.x.

J. Capon. High-Resolution Frequency-Wavenumber Spectrum Analysis. *Proceedings of the IEEE*, 57(8):1408–1418, 1969.

CEN. *Eurocode 8: Design of structures for earthquake resistance - Part 1: General rules, seismic actions and rules for buildings*. European Committee for Standardization, en 1998-1: edition, 2004.

Donat Fäh, Fortunat Kind, and Domenico Giardini. A theoretical investigation of average H / V ratios. *Geophysical Journal International*, 145:535–549, 2001.

Donat Fäh, Gabriela Stamm, and Hans-Balder Havenith. Analysis of three-component ambient vibration array measurements. *Geophysical Journal International*, 172(1):199–213, January 2008. ISSN 0956540X. doi: 10.1111/j.1365-246X.2007.03625.x. URL http://doi.wiley.com/10.1111/j.1365-246X.2007.03625.x.

Donat Fäh, Marc Wathelet, Miriam Kristekova, Hans-Balder Havenith, Brigitte Endrun, Gabriela Stamm, Valerio Poggi, Jan Burjanek, and Cécile Cornou. Using Ellipticity Information for Site Characterisation Using Ellipticity Information for Site Characterisation. Technical report, NERIES JRA4 Task B2, 2009.

Corine Frischknecht, Philippe Rosset, and Jean-Jacques Wagner. Toward Seismic Microzonation,Äî2-D Modeling and Ambient Seismic Noise Measurements: The Case of an Embanked, Deep Alpine Valley. *Earthquake Spectra*, 21(3):635, 2005. ISSN 87552930. doi: 10.1193/1.1941252. URL http://link.aip.org/link/EASPEF/v21/i3/p635/s1\&Agg=doi.

Stefan Fritsche. *Large Historical Earthquakes in Switzerland Multidisciplinary Studies on Damage Fields and Site-Effects*. PhD thesis, ETH Zurich, 2008.

GéoVal Ingénieurs. Microzonage sismique spectral de la région de Sion, Secteur A - Sion agglomération, Rapport géologique. Technical report, Sion, 2011.

William B. Joyner, Richard E. Warrick, and Thomas E. Fumal. The effect of Quaternary alluvium on strong ground motion in the Coyote Lake, California, earthquake of 1979. *Bulletin of the Seismological Society of America*, 71(4):1333–1349, 1981.

Katsuaki Konno and Tatsuo Ohmachi. Ground-Motion Characteristics Estimated from Spectral Ratio between Horizontal and Vertical Components of Microtremor. *Bulletin of the Seismological Society of America*, 88(1):228–241, 1998.

Valerio Poggi and Donat Fäh. Estimating Rayleigh wave particle motion from three-component array analysis of ambient vibrations. *Geophysical Journal International*, 180(1):251–267, January 2010. ISSN 0956540X. doi: 10.1111/j.1365-246X.2009.04402.x. URL http://doi.wiley.com/10.1111/j.1365-246X.2009.04402.x.

J.M. Roesset. Fundamentals of soil amplification. In R. J. Hansen, editor, *Seismic Design for Nuclear Power Plants*, pages 183–244. M.I.T. Press, Cambridge, Mass., 1970. ISBN 978-0-262-08041-5. URL http://mitpress.mit.edu/catalog/item/default.asp?ttype=2\&tid=5998.

Alberto Rosselli. *Modélisation gravimétrique bi- et tridimensionnelle du substratum rocheux des vallées alpines - Applications à la Vallée du Rhône (Suisse), à la vallée de l'Adige (Italie) et au glacier de Lobbia (Italie).* PhD thesis, Université de Lausanne, 2001.

Daniel Roten. *Site effects in the Rhone valley analysed by ambient noise, weak motion records and numerical simulations*. PhD thesis, ETH Zürich, 2007.

Daniel Roten, Donat Fäh, Cécile Cornou, and Domenico Giardini. Two-dimensional resonances in Alpine valleys identified from ambient vibration wavefields. *Geophysical Journal International*, 165(3):889–905, June 2006. ISSN 0956540X. doi: 10.1111/j.1365-246X.2006.02935.x. URL http://doi.wiley.com/10.1111/j.1365-246X.2006.02935.x.

Daniel Roten, Donat Fäh, K. B. Olsen, and Domenico Giardini. A comparison of observed and simulated site response in the Rhône valley. *Geophysical Journal International*, 173 (3):958–978, June 2008. ISSN 0956540X. doi: 10.1111/j.1365-246X.2008.03774.x. URL http://doi.wiley.com/10.1111/j.1365-246X.2008.03774.x.

SIA. *SIA 261 Actions sur les structures porteuses*. Société suisse des ingénieurs et des architectes, Zürich, sia 261:20 edition, 2003.

Marc Wathelet. An improved neighborhood algorithm: Parameter conditions and dynamic scaling. *Geophysical Research Letters*, 35(9):1–5, May 2008. ISSN 0094-8276. doi: 10.1029/2008GL033256. URL http://www.agu.org/pubs/crossref/2008/2008GL033256.shtml.